Analysis, Design, and Implementation of WPT System for EV's Battery Charging Based on Optimal Operation Frequency Range

Yongbin Jiang, *Student Member, IEEE*, Laili Wang, *Senior Member, IEEE*, Yue Wang, *Member, IEEE*, Junwen Liu, Min Wu, and Gaidi Ning

***Abstract*—Charging electric vehicles wirelessly is promising because of its convenience as well as saving of charging cables. However, the existing wireless power transfer systems suffer from high resonant peaks and poor efficiency. Therefore, zero voltage switching (ZVS) operation of inverter should be achieved especially in high transfer power. Based on the variable frequency phase shift control strategy (VFPSC), this paper presents an optimal operation frequency range (OOFR) where the wireless power transfer (WPT) system can realize the required output and ZVS operation of inverter simultaneously without extra dc–dc converters. Meanwhile, based on OOFR, an optimized electrical parameter design method based on VFPSC is proposed with the multiple boundary conditions. Moreover, a novel three-loop control strategy (TLCS) is proposed to make the system operate at any points of OOFR. Especially, an implementation method of the TLCS is proposed, which can dynamically adjust frequency and phase shift to make the system always operate at the preset ZVS angle and realize the required output simultaneously. Finally, a 500-W WPT system is built to verify the correctness of theoretical analysis. The experimental results show that a very high overall efficiency is achieved in the whole charging process and the maximum efficiency can achieve 94.9% with $k = 0.2$.**

***Index Terms*—Optimal operation frequency range (OOFR), parameter design, variable frequency phase shift control (VFPSC), wireless power transfer system (WPTS), zero voltage switching (ZVS).**

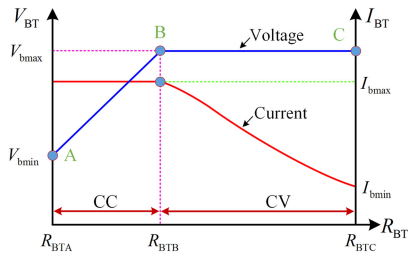

I. Introduction

WIRELESS power transfer (WPT) that uses magnetic field to deliver power efficiently has been applied to many applications including biomedical implants [1]–[4], consumer electronics [5]–[7], underwater loads [8], [9], electrical vehicles

Manuscript received February 9, 2018; revised May 10, 2018 and July 20, 2018; accepted September 13, 2018. Date of publication September 30, 2018; date of current version May 2, 2019. This work is supported by the National Key R&D Program of China under Grant 2018YFB0106300, the Fundamental Research Funds for the Central Universities under Grant xjj2018186 and the Young Scientists Fund of the National Natural Science Foundation of China under Grant 51607141, in part by the State Key Laboratory of Electrical Insulation and Power Equipment, Xi'an Jiaotong University. Recommended for publication by Associate Editor A. Khaligh. *(Corresponding author: Yue Wang.)*

The authors are with the State Key Laboratory of Electrical Insulation and Power Equipment, Xi'an Jiaotong University, Xi'an 710049, China (e-mail:

zero voltage switching (ZVS) operation in the whole charging process [28]–[31]. To realize these two control aims, many researchers have made great efforts and proposed numerous control methods. They can be divided into four major types. The first type is the pure phase shift control [26], [32]. This control method can realize constant output current or voltage by adjusting the phase shift angle, but it cannot realize ZVS operation of inverter in the whole charging process. The second type is the frequency control and its typical application is the self-oscillating control strategy [27], [33]. This control method adjusts the output current or voltage and realizes ZVS operation by regulating the operation frequency of inverter. However, the operation frequency is usually away from resonant frequency. Therefore, the reactive power is large and the overall efficiency is relatively poor. The third type mainly combines some dc–dc converters with the basic resonant topologies [34]–[36]. In these papers, the authors present a novel control structure using two dc–dc converters to realize adjustable output, ZVS operation, and impedance matching simultaneously. However, this method needs extra dc–dc converters, which augment the whole system cost and the overall efficiency of the whole system is also relatively poor. The fourth type is the pulsewidth modulation (PWM) control with phase-locked loop [30], [31]. This method can realize ZVS operation and constant output, but the ZVS angle (ZVSA) is fixed and cannot be adjusted flexibly. Meanwhile, this method lacks of systematic analysis and parameter design for CC/CV battery charging, and the operation frequency range (OFR) to realize the required output and ZVS operation has not been studied.

According to the above analysis and summary, this paper adopts the variable frequency phase shift control strategy (VFPSC) to control inverter flexibly. Based on VFPSC, this paper presents an optimal OFR (OOFR) where the WPTS can realize the required charging current or voltage for the battery packs and ZVS operation of inverter simultaneously without extra dc–dc converters. Meanwhile, on the basis of VFPSC and OOFR, an optimized electrical parameter design method is proposed with the multiple boundary conditions. Moreover, a novel three-loop control strategy (TLCS) by adding a decoupled ZVSA loop is put forward to make the system operate at any point of OOFR. An implementation method of the TLCS is proposed, which can dynamically adjust frequency and phase shift to make the system always operate at the preset ZVSA and realize the required output simultaneously. Finally, a 500-W WPTS is built to verify the correctness of theoretical analysis. The experimental results show that a very high overall efficiency is achieved in the whole charging process and the maximum efficiency can reach 94.9% with $k = 0.2$ and 94.1% with $k = 0.15$.

Section II presents a battery charging case-study and introduces the control targets and some basic concepts by using VFPSC in the WPTS. Section III proposes an optimized electrical parameter design method based on the multiple boundary conditions. Section IV finds out the OOFR to realize the required CC/CV output and ZVS operation simultaneously from the closed-loop perspective. Section V proposes an implementation method of the TLCS to make the system operate at any point in the OOFR. Section VI builds a 500-W experimental prototype. The steady-state and dynamic performances of the whole system are testified. Finally, Section VII concludes the paper.

TABLE I
BATTERY PARAMETERS AND SPECIFICATION

Symbol	Quantity	Value
V_{b1}	single module voltage	6.4 V-14.4 V
Q_{b1}	single module capacity	$40\ \mathrm{A}\cdot\mathrm{h}$
N	number of battery packs	5
V_{b}	overall module voltage	32 V-72 V
I_{bmax}	maximum charging current	4 A
I_{bmin}	floating charging current	1 A
R_{BTA}	load resistance in point A	8 Ω
R_{BTB}	load resistance in point B	18 Ω
R_{BTC}	load resistance in point C	72 Ω

II. BATTERY CASE-STUDY AND ANALYSIS OF WPTS

A. Battery Charging Case-Study

The WPT battery charger is designed around the charging profile of the battery packs of electric vehicles. In this paper, the battery packs are made of five lead-acid modules connected in series; the nominal capacity and voltage of a single module are $40\ \mathrm{A}\cdot\mathrm{h}$ and 12 V. The limit of the practical voltage of a single battery pack is set from 6.4 to 14.4 V and the overall voltage ranges from 32 to 72 V. The maximum charging current of battery pack is set as 4 A. The detailed specifications are listed in Table I. According to Fig. 1, in CC mode, the charging current maintains constant, and the battery voltage gradually increases from 32 to 72 V. The corresponding equivalent resistance of battery packs increases from R_{BTA} (8 Ω) to R_{BTB} (18 Ω). Once the charging voltage reaches the maximum value, the WPTS goes into the CV mode. The charging voltage maintains 72 V and the charging current gradually decreases from 4 to 1 A. Therefore, the corresponding equivalent resistor of battery packs increases from R_{BTB} (18 Ω) to R_{BTC} (72 Ω).

B. System Control Targets

As a kind of power supply for EV's batteries, the WPTS should first ensure the stable output current or voltage. To simplify the whole system structure, reduce cost, and save money, the common WPTS with series–series (SS) resonant network is applied, which is shown in Fig. 2(a). Moreover, to enhance the system efficiency and reduce electro-magnetic interference (EMI), the system control targets at achieving CC or CV charging for battery packs and realizing ZVS operation of primary inverter simultaneously. In this paper, VFPSC is applied in the primary inverter. When the SS resonant network is adopted and the frequency regulation method is applied, the range for frequency regulation is relatively narrow because the gain characteristics of this compensation topology are sensitive to the operation frequency. However, it is this frequency sensitivity that can help to change the impedance

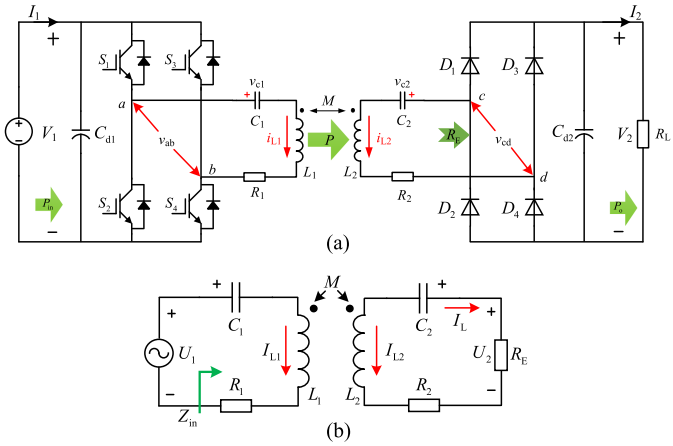

Fig. 2. (a) Full-bridge type WPTS using SS compensation. (b) Corresponding fundamental harmonic equivalent circuit.

characteristics of the resonant network and make the inverter realize ZVS operation within a small frequency range. Generally speaking, by using the two control variables: phase shift angle and operation frequency of the primary inverter, these two control targets can be realized simultaneously.

C. System Structure and Equivalent circuits

In Fig. 2(a), V_1 and I_1 are the dc input voltage and current of primary inverter, respectively. V_2 and I_2 are the dc output voltage and current of secondary rectifier, respectively. L_1 and L_2 are the self-inductances of the primary resonant coil and the secondary resonant coil, respectively. M is the mutual inductance and the coupling coefficient k is defined as $k = M/\sqrt{L_1 L_2}$. To minimize the reactive power in the resonant tanks and enhance the magnetic field produced by coils, the resonant capacitors C_1 and C_2 are added in the resonant circuit. For simplicity, the primary resonant frequency ω_1 and the secondary resonant frequency ω_2 are set to be equal to ω_0 (the resonant frequency of WPTS), which satisfy

$$\begin{cases} \omega_1 = \dfrac{1}{\sqrt{L_1 C_1}},\ \omega_2 = \dfrac{1}{\sqrt{L_2 C_2}} \\ \omega_0 = \omega_1 = \omega_2. \end{cases} \tag{1}$$

To study VFPSC more clearly and intuitively, the per-unit value of the operation frequency is defined as

$$\omega_{\mathrm{n}} = \omega_{\mathrm{s}}/\omega_0. \tag{2}$$

In the analysis of the WPTS, the fundamental harmonic approximation is normally used since the resonant fundamental current is considerably larger than harmonics [26], [35], [36]. The corresponding fundamental component equivalent circuit is depicted in Fig. 2(b). V_1 and I_1 are the input dc voltage and current; V_2 and I_2 are the output dc voltage and current. U_1 and U_2 are the rms values of the fundamental harmonics of the ac input voltage v_{ab1} and the ac output voltage v_{cd1}, respectively; I_{L1} and I_{L2} are the rms values of the primary and secondary inductor currents, respectively; V_{c1} and V_{c2} are the rms values of the primary and secondary resonant capacitor voltages, respectively; R_1 and R_2 are used to stand for the equivalent series resistors (ESRs) of the primary resonant network and the secondary one.

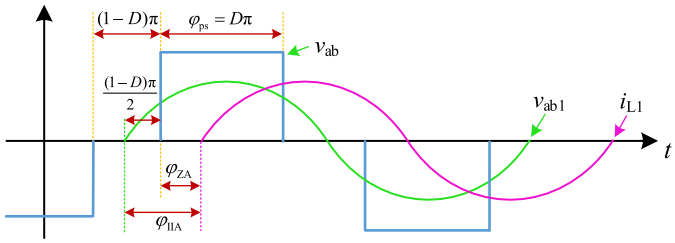

Fig. 3. Operation waveforms of primary inverter.

D. Variable Frequency Phase Shift Control

To adjust the system output and realize ZVS operation of the inverter, VFPSC is applied. The operation waveforms of primary inverter are shown in Fig. 3. v_{ab1} is the fundamental waveform of ac output voltage of inverter v_{ab} with phase shift angle φ_{ps} ($\varphi_{\mathrm{ps}} = D\pi$), and i_{L1} is the primary inductor current. Consequently, the phase between v_{ab1} and i_{L1} is the input impedance angle (IIA) of resonant network, φ_{IIA}. Meanwhile, the angle for ZVS operation is defined as φ_{ZA}. Generally speaking, when $\varphi_{\mathrm{ZA}} \geq 0$, the inverter can realize ZVS operation.

According to the fundamental harmonic analysis, the rms value of v_{ab1} can be calculated by

$$U_1 = \frac{2\sqrt{2}}{\pi} V_1 \sin\left[\frac{D\pi}{2}\right]. \tag{3}$$

For the full-bridge rectifier, the rms value of v_{cd2} and i_{L2} can be obtained by

$$\begin{cases} U_2 = \dfrac{2\sqrt{2}}{\pi} V_2 \\ I_{\mathrm{L2}} = \dfrac{\pi}{2\sqrt{2}} I_2. \end{cases} \tag{4}$$

According to power conservation, the rectifier can be replaced by an equivalent load resistance R_{E} which satisfies

$$R_{\mathrm{E}} = \frac{8}{\pi^2} R_{\mathrm{L}}. \tag{5}$$

Therefore, the load quality factor Q_{s} can be obtained by [37]

$$Q_{\mathrm{s}} = \frac{\omega_{\mathrm{s}} L_2}{R_{\mathrm{E}}} = \frac{\pi^2 \omega_{\mathrm{s}} L_2}{8 R_{\mathrm{L}}}. \tag{6}$$

E. Input Impedance Angle

As shown in Fig. 2(b), according to [25], the input impedance of resonant network is given as

$$Z_{\mathrm{in}} = Z_1 + \omega^2 M^2/(Z_2 + R_{\mathrm{E}}) \tag{7}$$

where Z_2 is the secondary resonant network impedance, which is $Z_2 = R_2 + j\omega_{\mathrm{s}} L_2 + 1/j\omega_{\mathrm{s}} C_2$ and Z_1 is the primary resonant network impedance, which is $Z_1 = R_1 + j\omega_{\mathrm{s}} L_1 + 1/j\omega_{\mathrm{s}} C_1$. With R_1 and R_2 neglected [38], the input impedance angle can

TABLE II
SYSTEM PARAMETERS USED IN CALCULATION

Symbol	Quantity	Value
L_1, L_2	resonant inductances	116.86μH
C_1, C_2	resonant capacitances	30nF
k	coupling coefficiency	0.15-0.2
ω_0	resonant angular frequency	5.34×10^5rad/s
f_0	resonant frequency	85kHz
R_{L}	load resistance	10Ω

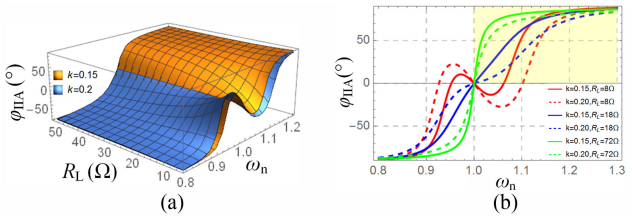

Fig. 4. Characteristics of φ_{IIA}. (a) $k = 0.15$, 0.2, with different R_{L} and ω_{n}. (b) $k = 0.15$, 0.2 and $R_{\mathrm{L}} = 8\ \Omega$, 18 Ω, 72 Ω, respectively, with different ω_{n}.

be calculated by

$$\varphi_{\mathrm{IIA}} = \frac{180}{\pi}\arctan\left[\frac{\mathrm{Im}\left[Z_{\mathrm{in}}\right]}{\mathrm{Re}\left[Z_{\mathrm{in}}\right]}\right] = -\frac{180}{\pi}\arctan\left[\frac{\left(-1+\omega_{\mathrm{n}}^2\right)\left(-64R_{\mathrm{L}}^2\omega_{\mathrm{n}}^2+\pi^4L_2^2\omega_0^2\left(-1+2\omega_{\mathrm{n}}^2+\left(-1+k^2\right)\omega_{\mathrm{n}}^4\right)\right)}{8\pi^2k^2L_2R_{\mathrm{L}}\omega_0\omega_{\mathrm{n}}^5}\right]. \tag{8}$$

With the parameters listed in Table II and different coupling coefficient, φ_{IIA} as a function of per-unit operation frequency ω_{n} and load resistance R_{L} is calculated and plotted in Fig. 4(a). When k and R_{L} are fixed, φ_{IIA} as a function of ω_{n} is plotted in Fig. 4(b). It shows that, as R_{L} increases, the relationship between φ_{IIA} and ω_{n} varies from single peak and single valley to monotonic increasing. Only when $\omega_{\mathrm{n}} > 1$ and $\varphi_{\mathrm{IIA}} > 0$ (as shown in yellow region), φ_{IIA} is a monotone increasing function of ω_{n}, which is crucial to ZVSA control.

F. Zero Voltage Switching Angle

Based on VFPSC, the output voltage and current waveforms of the primary inverter are shown in Fig. 3, where D represents the duty cycle of v_{ab} and $D\pi$ is the phase shift angle. The phase angle φ_{ZA} between the rising edge of v_{ab} and the zero-crossing point of i_{L1}, is defined as ZVSA. From Fig. 3, we can obtain

$$\varphi_{\mathrm{IIA}} = \varphi_{\mathrm{ZA}} + \frac{(1-D)\pi}{2}. \tag{9}$$

To reduce switching cost and EMI, and enhance the system efficiency and reliability, ZVS should be achieved in primary inverter, which means $\varphi_{\mathrm{ZA}} > 0$ at least. Usually, when D satisfies $1 > D > 0$, then $\varphi_{\mathrm{IIA}} > \varphi_{\mathrm{ZA}}$ is obtained. According to Fig. 4(b) and (9), to provide positive φ_{ZA}, the essential condition is $\varphi_{\mathrm{IIA}} > 0$. Therefore, to ensure the monotonic increasing character of φ_{IIA} when $\varphi_{\mathrm{IIA}} > 0$, the best choice for OFR is $\omega_{\mathrm{n}} > 1$, which is vital for ZVSA control.

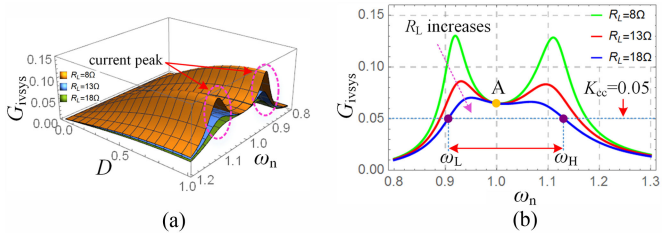

Fig. 5. TCGS with $k = 0.2$. (a) G_{ivsys} as a function of D and ω_{n}. (b) G_{ivsys} as a function of ω_{n} when $D = 1$.

III. SYSTEM CHARACTERISTICS ANALYSIS AND RESONANT TANK PARAMETER DESIGN

In this section, to satisfy the required current and voltage for the battery packs listed in Table I, the system characteristics are analyzed in detail and the resonant parameters are designed.

A. Trans-Conductance Gain of the System (TCGS)

Based on Fig. 2(b) with $R_1 = R_2 = 0\ \Omega$, the trans-conductance gain of resonant network can be obtained by

$$G_{\mathrm{ivss}} = \frac{I_{\mathrm{L2}}}{U_1} = \frac{kL_2\omega_{\mathrm{n}}^3}{\sqrt{L_1L_2\left(R_{\mathrm{E}}^2\omega_{\mathrm{n}}^2\left(\omega_{\mathrm{n}}^2-1\right)^2+\omega_0^2L_2^2\left(-1+2\omega_{\mathrm{n}}^2+\left(-1+k^2\right)\omega_{\mathrm{n}}^4\right)^2\right)}}. \tag{10}$$

To acquire the relationship between control variables D, ω_{n}, and control aim I_2, the TCGS is defined as

$$G_{\mathrm{ivsys}} = \frac{I_2}{V_1} = f(k, R_{\mathrm{L}}, \omega_{\mathrm{n}}, D). \tag{11}$$

Substituting (3)–(5) to (11), we can obtain (12) as shown at bottom of the page.

With the parameters listed in Table II, G_{ivsys} as a function of D and ω_{n} is calculated and plotted in Fig. 5(a). In a fixed R_{L}, G_{ivsys} will increase as D increases. To show the relationship between G_{ivsys} and ω_{n} more visually, when D is set to a certain value ($D = 1$), G_{ivsys} as a function of ω_{n} is plotted in Fig. 5(b). Once the resonant parameters and the required TCGS (represented by K_{cc}) are assured, the OFR from ω_{L} to ω_{H} gradually shrinks as R_{L} gradually increases. When the operation

$$G_{\mathrm{ivsys}} = \frac{I_2}{V_1} = \frac{8}{\pi^2}\sin\left[\frac{D\pi}{2}\right]G_{\mathrm{ivss}} = \frac{8kL_2\omega_{\mathrm{n}}^3\sin\left[D\pi/2\right]}{\sqrt{L_1L_2\left(64R_{\mathrm{L}}^2\omega_{\mathrm{n}}^2\left(-1+\omega_{\mathrm{n}}^2\right)^2+\pi^4L_2^2\omega_0^2\left(-1+2\omega_{\mathrm{n}}^2+\left(-1+k^2\right)\omega_{\mathrm{n}}^4\right)^2\right)}} \tag{12}$$

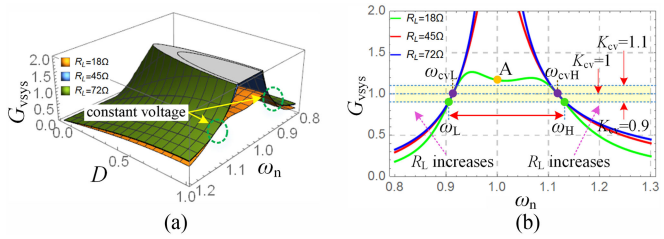

Fig. 6. VGS with $k = 0.2$, (a) G_{vsys} as a function of D and ω_{n} and (b) G_{vsys} as a function of ω_{n} when $D = 1$.

frequency is set as $\omega_{\mathrm{n}} = 1$, the charging current I_2 is independent of the load resistance R_{L}. Therefore, in consideration of the regularity that G_{ivsys} increases as D increases and decreases as R_{L} increases, to ensure the existence of the OFR, the maximum G_{ivsys} at point A ($D = 1$, $\omega_{\mathrm{n}} = 1$) predetermined by circuit design should be larger than the one that battery packs need in CC mode. According to (12), at point A, the maximum value of G_{ivsys} with $\omega_{\mathrm{n}} = 1$ can be obtained by

$$G_{\mathrm{ivsys}}(D = 1,\ \omega_{\mathrm{n}} = 1) = \frac{8}{\pi^2 \omega_0 k \sqrt{L_1 L_2}}. \tag{13}$$

B. Voltage Gain of the System (VGS)

Similarly, based on Fig. 2(b) with $R_1 = R_2 = 0\,\Omega$, the voltage gain of resonant network can be obtained by

$$G_{\mathrm{vss}} = \frac{U_2}{U_1} = \frac{k L_2 R_{\mathrm{E}} \omega_{\mathrm{n}}^3}{\sqrt{L_1 L_2 \left(R_{\mathrm{E}}^2 \omega_{\mathrm{n}}^2 (-1+\omega_{\mathrm{n}}^2)^2 + L_2^2 \omega_0^2 (-1+2\omega_{\mathrm{n}}^2 + (-1+k^2)\,\omega_{\mathrm{n}}^4)^2\right)}}. \tag{14}$$

To acquire the relationship between control variables D, ω_{n}, and control aim V_2, the VGS can be defined as

$$G_{\mathrm{vsys}} = \frac{V_2}{V_1} = f(k, R_{\mathrm{L}}, \omega_{\mathrm{n}}, D). \tag{15}$$

Substituting (3)–(5) in (15), we can obtain (16) as shown at bottom of the page.

With the parameters listed in Table II, G_{vsys} as a function of D and ω_{n} is calculated and plotted in Fig. 6(a). Similarly, G_{vsys} will increase as D increases. The maximum value of G_{vsys} gradually increases as R_{L} increases. To show the relationship between G_{vsys} and ω_{n} more visually, when D is set to a certain value ($D = 1$), G_{vsys} as a function of ω_{n} is plotted in Fig. 6(b) and the required VGS is represented by K_{cv}. It can be seen that G_{vsys} is independent of R_{L} when $\omega_{\mathrm{n}} = \omega_{\mathrm{cvL}}$ or $\omega_{\mathrm{n}} = \omega_{\mathrm{cvH}}$. Therefore, the basic design point is that the OFR of the practical system should include the yellow region to satisfy the CV charging and obtain better voltage regulation performance. Therefore, to ensure the existence of the OFR with R_{L} ranging from R_{BTB} to R_{BTC}, G_{vsys} at the point of ω_{cvH} predetermined by circuit design should be larger than the one that battery packs need in CV mode. When $\omega_{\mathrm{n}} = \omega_{\mathrm{cvH}}$ or $\omega_{\mathrm{n}} = \omega_{\mathrm{cvL}}$ and $D = 1$, the maximum value of G_{vsys} can be obtained by

$$G_{\mathrm{vsys}}(\omega_{\mathrm{n}} = \omega_{\mathrm{cvL}} \text{or } \omega_{\mathrm{n}} = \omega_{\mathrm{cvH}} \text{ and } D = 1) = \sqrt{\frac{L_2}{L_1}} \tag{17}$$

where

$$\omega_{\mathrm{cvL}} = \frac{1}{\sqrt{1+k}} \text{ and } \omega_{\mathrm{cvH}} = \frac{1}{\sqrt{1-k}}. \tag{18}$$

C. Resonant Current and Voltage

In the whole charging process, the maximum rms values of the resonant currents in the coils and the resonant voltages in the capacitors should be evaluated. This discussion about the resonant currents and voltages can be divided into two parts: the primary side and the secondary side.

1) In the Secondary Side: According to (4), the rms values of the secondary resonant current i_{L2} and the resonant voltage v_{c2} can be obtained by

$$\begin{cases} I_{\mathrm{L2}} = \dfrac{\pi}{2\sqrt{2}} I_2 \\ V_{\mathrm{c2}} = \dfrac{1}{\omega_{\mathrm{s}} C_2} I_{\mathrm{L2}}. \end{cases} \tag{19}$$

According to (19), in the secondary side, the resonant current I_{L2} only depends on the output dc current I_2 and is independent of the operation frequency. In CC mode, I_{L2} maintains constant and achieves the maximum value. Therefore, the secondary side coil is designed by only considering the maximum charging current in CC mode. Substituting (1) and (2) into (19), V_{c2} can be obtained by

$$V_{\mathrm{c2}} = \frac{\pi I_2 L_2 \omega_0}{2\sqrt{2}\omega_{\mathrm{n}}}. \tag{20}$$

Obviously, V_{c2} achieves the maximum value with the maximum I_2 and the minimum ω_{n}. Once the operation range of ω_{n} and the maximum I_2 are confirmed, the maximum value of V_{c2} can be easily calculated.

2) In the Primary Side: To acquire the primary resonant current, the current gain of resonant network should be obtained. Based on Fig. 2(b) and neglecting R_1 and R_2, the current gain of resonant network can be obtained by

$$G_{\mathrm{iss}} = \frac{I_{\mathrm{L2}}}{I_{\mathrm{L1}}} = \frac{k\sqrt{L_1 L_2}\omega_0 \omega_{\mathrm{n}}^2}{\sqrt{\omega_{\mathrm{n}}^2 R_{\mathrm{E}}^2 + \omega_0^2 L_2^2 (1-\omega_{\mathrm{n}}^2)^2}}. \tag{21}$$

According to (19) and (21), the rms values of the primary resonant current i_{L1} and the resonant voltage v_{c1} can be obtained

$$G_{\mathrm{vsys}} = \frac{V_2}{V_1} = \sin\left[\frac{D\pi}{2}\right] G_{\mathrm{vss}} = \frac{8 k L_2 R_{\mathrm{L}} \omega_{\mathrm{n}}^3 \sin[D\pi/2]}{\sqrt{L_1 L_2 \left(64 R_{\mathrm{L}}^2 \omega_{\mathrm{n}}^2 (-1+\omega_{\mathrm{n}}^2)^2 + \pi^4 L_2^2 \omega_0^2 (-1+2\omega_{\mathrm{n}}^2 + (-1+k^2)\,\omega_{\mathrm{n}}^4)^2\right)}} \tag{16}$$

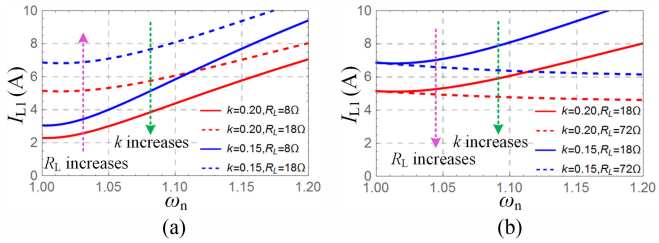

Fig. 7. Primary resonant current, I_{L1}, with $k = 0.2$ and 0.15. (a) In CC charging mode with $I_2 = 4$ A. (b) In CV charging mode with $V_2 = 72$ V.

TABLE III
PARAMETER DESIGN SPECIFICATIONS

Symbol	Quantity	Value
V_1	input dc voltage of inverter	80 V
f_0	resonant frequency	85 kHz
ω_0	resonant angular frequency	5.34×10^5 rad/s
ω_n	per-unit operation frequency of inverter	$1 - 1.3$
k	coupling coefficiency	0.15-0.2
η_{iv}	the factor of current allowance	1.2
K_{cc}	the required trans-conductance gain	0.05
K_{cv}	the range of the required voltage gain	0.9-1.1
Q_{smin}	the minimum load quality factor	1
I_{L1max}	the primary maximum resonant current	8.5 A
V_{c1max}	the primary maximum resonant voltage	480 V
V_{c2max}	the secondary maximum resonant voltage	350 V
R_L	load resistance	$8\,\Omega - 72\,\Omega$

by

$$\begin{cases} I_{L1} = \dfrac{I_2\sqrt{64R_L^2\omega_n^2 + \pi^4\omega_0^2L_2^2(\omega_n^2-1)^2}}{2\sqrt{2}\pi k\sqrt{L_1L_2}\omega_0\omega_n^2} \\ V_{c1} = \dfrac{I_2L_1\sqrt{64R_L^2\omega_n^2 + \pi^4\omega_0^2L_2^2(\omega_n^2-1)^2}}{2\sqrt{2}\pi k\sqrt{L_1L_2}\omega_n^3}. \end{cases} \tag{22}$$

With the parameters listed in Table II, I_{L1} as a function of ω_n is calculated and plotted in Fig. 7. As shown in Fig. 7, on the one hand, in a fixed operation frequency ω_n, the resonant current I_{L1} is the monotonic increasing function of R_L in CC charging mode and the monotonic decreasing function of R_L in CV charging mode. On the other hand, I_{L1} is always the monotonic decreasing function of the coupling coefficient k. Generally speaking, when the WPTS operates in point B ($R_L = R_{BTB}$) with the lowest coupling coefficient, I_{L1} reaches the maximum value. Similarly, the resonant voltage V_{c1} has the same situations.

D. Parameters Design

Before the parameter design, the related parameter specifications of the operation condition should be confirmed, which are listed in Table III. In this section, we should consider five conditions that are the required charging current, the required charging voltage, the minimum value of quality factor, the resonant currents of coils, and the resonant voltages of capacitors. Next, we will discuss these five conditions in detail.

1) Required Charging Current: According to the battery parameters in Table I, in CC mode, the required TCGS can be calculated, $K_{cc} = I_2/V_1 = 0.05$. In consideration of the system loss, the designed parameters of resonant network should remain a certain output current margin, which can be represented by a factor η_{iv}. According to the previous analysis in Section III-A and (13), we can get

$$G_{ivsys}(D = 1,\ \omega_n = 1) = \frac{8}{\pi^2\omega_0 k\sqrt{L_1L_2}} > K_{cc} \times \eta_{iv}. \tag{23}$$

By solving (23), the range of L_1 can be obtained, which is

$$0 < L_1 < \frac{64}{\pi^4\eta_{iv}^2K_{cc}^2k^2\omega_0^2L_2}. \tag{24}$$

With $\eta_{iv} = 1.2$ and the parameters listed in Table III, the maximum value of L_1 can be obtained.

2) Required Charging Current: According to the battery parameters in Table I, in CV mode, the required VGS can be calculated, $K_{cv} = V_2/V_1 = 0.9$. In consideration of the system loss, the designed parameters of resonant network should remain a certain output voltage margin. As shown in Fig. 6, based on the previous analysis in Section III-B, the range of G_{vsys} should be set as $K_{cvmin} - K_{cvmax}$ and the center point of this range can be set as the constant VGS with $\omega_n = \omega_{cvL}$ or $\omega_n = \omega_{cvH}$. Then, based on (17), we can get

$$K_{cvmax} > \sqrt{\frac{L_2}{L_1}} > K_{cvmin}. \tag{25}$$

Similarly, by solving (25), the range of L_1 can be obtained, which is

$$\frac{L_2}{K_{cvmin}^2} > L_1 > \frac{L_2}{K_{cvmax}^2}. \tag{26}$$

With the parameters listed in Table III, the maximum and minimum values of L_1 can be obtained.

3) Minimum Value of Quality Factor: The system efficiency is affected by the quality factor of load [37]. Larger Q_s is beneficial for enhancing the system efficiency. Therefore, there is a lower limitation of permitted Q_s signed as Q_{smin}, by using VFPSC. Then, based on the (5) and (6), we can get

$$\frac{\pi^2\omega_n\omega_0L_2}{8R_L} > Q_{s\,min}. \tag{27}$$

By solving (27), the range of L_2 can be obtained, namely

$$L_2 > \frac{8R_LQ_{smin}}{\pi^2\omega_n\omega_0}. \tag{28}$$

With the parameters listed in Table III and ω_n, the minimum value of L_2 can be obtained.

4) Secondary Resonant Current and Voltage: The secondary resonant current and voltage can be evaluated easily. According to the previous analysis in Section III-C, I_{L2} can be easily confirmed and V_{c2} is the resonant voltage, which should be smaller than the preset maximum value V_{c2max}, that is

$$V_{c2} = \frac{\pi I_2L_2\omega_0}{2\sqrt{2}\omega_n} < V_{c2max}. \tag{29}$$

TABLE IV
PARAMETER DESIGN RANGE

No	Symbol	Quantity	Value
1	the required charging current	$G_{\mathrm{ivsys}}(D=1\text{and }\omega_{\mathrm{n}}=1)>\eta_{\mathrm{iv}}\times K_{\mathrm{cc}}$	$0<L_1<\frac{64}{\pi^4\eta_{\mathrm{iv}}^2K_{\mathrm{cc}}^2k^2\omega_0^2L_2}$
2	the required charging voltage	$\begin{cases} G_{\mathrm{vsys}}(\omega_{\mathrm{cvL}}\text{or }\omega_{\mathrm{cvH}}\text{ and }D=1)=\sqrt{L_2/L_1} \\ K_{\mathrm{cvmax}}>\sqrt{L_2/L_1}>K_{\mathrm{cvmin}} \end{cases}$	$\frac{L_2}{K_{\mathrm{cvmin}}^2}>L_1>\frac{L_2}{K_{\mathrm{cvmax}}^2}$
3	the minimum value of quality factor	$Q_{\mathrm{s}}(\omega_{\mathrm{n}}=1)>Q_{\mathrm{s\,min}}$	$L_2>\frac{8R_{\mathrm{L}}Q_{\mathrm{smin}}}{\pi^2\omega_{\mathrm{n}}\omega_0}$
4	the secondary resonant voltage and current	$\begin{cases} I_{\mathrm{L2}}<I_{\mathrm{L2max}} \\ V_{\mathrm{c2}}<V_{\mathrm{c2max}} \end{cases}$	$L_2<\frac{2\sqrt{2}\omega_{\mathrm{n}}V_{\mathrm{c2max}}}{\pi I_2\omega_0}$
5	the primary resonant voltage and current	$\begin{cases} I_{\mathrm{L1}}(\omega_{\mathrm{n}}=\omega_{\mathrm{cvH}})<I_{\mathrm{L1max}} \\ V_{\mathrm{c1}}(\omega_{\mathrm{n}}=\omega_{\mathrm{cvH}})<V_{\mathrm{c1max}} \end{cases}$	$\begin{cases} L_1>\frac{I_2^2\left(64R_{\mathrm{L}}^2\omega_{\mathrm{n}}^2+\pi^4\omega_0^2L_2^2(\omega_{\mathrm{n}}^2-1)^2\right)}{8\pi^2k^2\omega_0^2L_2\omega_{\mathrm{n}}^4I_{\mathrm{L1max}}^2} \\ L_1<\frac{8\pi^2k^2\omega_0^2L_2\omega_{\mathrm{n}}^6V_{\mathrm{c1max}}^2}{I_2^2\left(64R_{\mathrm{L}}^2\omega_{\mathrm{n}}^2+\pi^4\omega_0^2L_2^2(\omega_{\mathrm{n}}^2-1)^2\right)} \end{cases}$

By solving (29), the range of L_2 can be obtained

$$L_2<\frac{2\sqrt{2}\omega_{\mathrm{n}}V_{\mathrm{c2max}}}{\pi I_2\omega_0}. \tag{30}$$

If the maximum value of V_{c2} and the minimum operation frequency are confirmed, the upper limit of the secondary inductance can be obtained based on the secondary maximum resonant voltage.

5) Primary Resonant Current and Voltage: The primary resonant current and voltage should be carefully evaluated. However, the derivations of the primary resonant current and voltage are very complicated when VFPSC is applied in WPTS for the whole charging process of battery. Due to the frequency sensitivity of the SS compensated WPTS, the practical adjustable frequency range is relatively narrow. In CC charging mode, as shown in Fig. 5(b), the operation frequency ω_{n} gradually moves toward the resonant frequency ($\omega_{\mathrm{n}}=1$) as the load R_{L} increases. When the WPTS enters into the CV charging mode and G_{vsys} equals to the required voltage gain K_{cv}, the upper operation frequency will stay near ω_{cvH}. According the previous design rules 1) and 2) of the required charging current and voltage, some reasonable assumptions should be made for simplicity.

1) Due to the frequency sensitivity of the SS compensated topology, the OFR used for the constant output is relatively narrow (in this paper $\omega_{\mathrm{n}}=1-1.3$).
2) The primary resonant current and voltage achieve the maximum values when the load resistor R_{L} equals R_{BTB} with the maximum charging power.
3) R_{BTB} is the starting point of the CV mode and the practical operation frequency is near ω_{cvH}.

Therefore, based on the related analysis in Section III-C and the three assumptions, we use the operation point B ($R_{\mathrm{L}}=R_{\mathrm{BTB}}$) with ω_{cvH} and lowest coupling to evaluate the maximum resonant current and voltage of the primary side in the whole charging process. Therefore, to limit the maximum value of the resonant current and voltage, we mainly consider the most serious condition (in point B: $I_2=4$ A, $V_2=72$ V, and $k=0.15$). Based on (22), if the maximum value of I_{L1} is set as I_{L1max}, we can get

$$I_{\mathrm{L1}}=\frac{I_2\sqrt{64R_{\mathrm{L}}^2\omega_{\mathrm{n}}^2+\pi^4\omega_0^2L_2^2(\omega_{\mathrm{n}}^2-1)^2}}{2\sqrt{2}\pi k\sqrt{L_1L_2}\omega_0\omega_{\mathrm{n}}^2}<I_{\mathrm{L1max}}. \tag{31}$$

By solving (31), the range of L_1 can be obtained

$$L_1>\frac{I_2^2\left(64R_{\mathrm{L}}^2\omega_{\mathrm{n}}^2+\pi^4\omega_0^2L_2^2\left(\omega_{\mathrm{n}}^2-1\right)^2\right)}{8\pi^2I_{\mathrm{L1max}}^2k^2\omega_0^2L_2\omega_{\mathrm{n}}^4}. \tag{32}$$

Similarly, based on (22), if the maximum resonant voltage of V_{c1} is set as V_{c1max}, we can get

$$V_{\mathrm{c1}}=\frac{I_2L_1\sqrt{64R_{\mathrm{L}}^2\omega_{\mathrm{n}}^2+\pi^4\omega_0^2L_2^2(\omega_{\mathrm{n}}^2-1)^2}}{2\sqrt{2}\pi k\sqrt{L_1L_2}\omega_{\mathrm{n}}^3}<V_{\mathrm{c1max}}. \tag{33}$$

By solving (33), the range of L_1 can be obtained

$$0<L_1<\frac{8\pi^2k^2L_2\omega_{\mathrm{n}}^6V_{\mathrm{c1max}}^2}{I_2^2\left(64R_{\mathrm{L}}^2\omega_{\mathrm{n}}^2+\pi^4\omega_0^2L_2^2(\omega_{\mathrm{n}}^2-1)^2\right)}. \tag{34}$$

Generally speaking, if the primary resonant inductor satisfies (32) and (34), both the resonant current I_{L1} and the resonant voltage V_{c1} will be limited to the reasonable range in the steady state. Because this design is based on the approximately worst situation (the maximum output current, the maximum output voltage, and the minimum coupling coefficient), this design result will satisfy other situations in the whole charging process approximately. Commonly, in the battery charging process, the related five requirements should be considered and the related parameter ranges limited by them for selection are summarized in Table IV .

6) Selected Range of Resonant Parameters: To satisfy all of the proposed design requirements, a resonant parameter design method based on the multiple boundary conditions is proposed. Based on the design ranges in Table IV and the parameters listed in Table III, the multiple boundary curves for resonant inductance selection are plotted in Fig. 8. The selection of the primary and secondary inductances should be limited to the yellow region where all the requirements listed in Table III can be satisfied. By the way, the parameters listed in Table I are exactly in the yellow region. The point P_{c} is used for theoretical calculation and P_{e} is the practical experimental point.

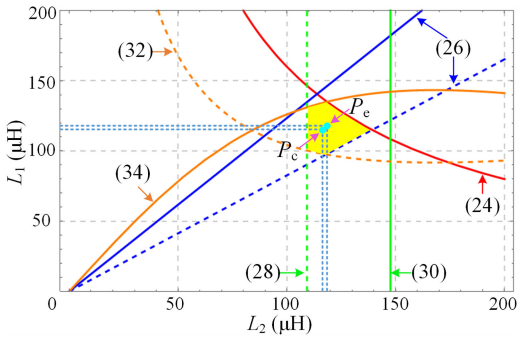

Fig. 8. Multiple boundary conditions and the yellow region for inductance selection.

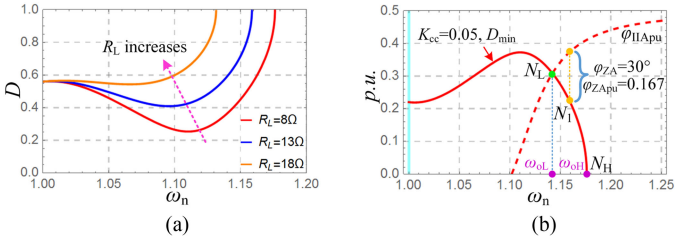

Fig. 9. (a) Relationship between D and ω_n, with $R_L = 8\ \Omega$, 13 Ω, and 18 Ω, when G_{ivsys} is maintained as 0.05. (b) Critical condition for ZVS and CC charging when $R_L = 8\ \Omega$ and $K_{cc} = 0.05$.

IV. Optimal Operation Frequency Range

The parameters have been selected for CC or CV charging for the battery and the corresponding OFR can be obtained easily. However, to reduce EMI and enhance the system efficiency, the ZVS operation of primary inverter should be realized. Therefore, OFR should be re-evaluated to find the appropriate operation frequency where the CC or CV charging and the ZVS operation of the primary inverter can be realized simultaneously. Undoubtedly, this special OFR is a part of OFR, which is called the OOFR.

A. CC Charging and ZVS Operation

When the input dc voltage V_1 and required charging current I_2 are fixed, the required K_{cc} is fixed accordingly. As shown in Fig. 5(a), there are many combinations between D and ω_n, which can realize CC charging. For example, to realize $G_{ivsys} = 0.05$ with $R_L = 8\ \Omega$, OFR ranges from ω_L to ω_H. Therefore, according to (12), if assigning that G_{ivsys} equals K_{cc}, the corresponding duty cycle D can be solved by (35) as shown at bottom of the page.

With the parameters listed in Table II, to maintain G_{ivsys} constant, the relationship curves between ω_n and D with different R_L, are plotted in Fig. 9(a). When R_L increases, the control variable D increases accordingly and the OFR of ω_n shrinks. However, in OFR, there are only parts of combinations between ω_n and D that can realize ZVS operation. According to (9), the

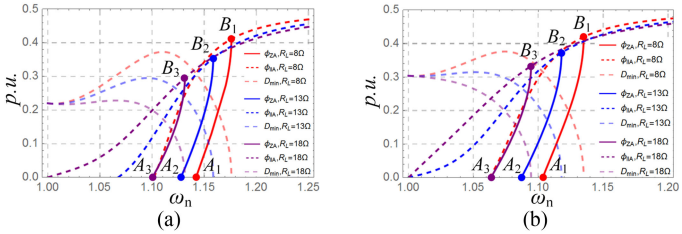

Fig. 10. OOFR is between A_x and B_x (x = 1, 2, 3), with $K_{cc} = 0.05$, $R_L = 8\ \Omega$, 13 Ω, 18 Ω. (a) $k = 0.2$. (b) $k = 0.15$.

critical conditions for ZVS operation when $\varphi_{ZA} = 0°$ can be obtained. That is

$$\varphi_{IIAmin} = (1 - D)\,\pi/2. \tag{36}$$

To display the relationships in identical picture, we define D_{min} and φ_{IIApu} as

$$\begin{cases} D_{min} = (1 - D)/2 \\ \varphi_{IIApu} = \varphi_{IIA}/180. \end{cases} \tag{37}$$

With the parameters listed in Table II, when $K_{cc} = 0.05$, D_{min} and φ_{IIApu} versus ω_n are plotted in Fig. 9(b). There are two intersection points: N_L and N_H. On the one hand, N_L is the intersection point between D_{min} and φ_{IIApu}, and the horizontal coordinate of N_L is the lower limit frequency ω_{oL}. In other words, when the operation frequency of the inverter is set as ω_{oL} and the phase shift angle of inverter is automatically adjusted to maintain the constant $K_{cc} = 0.05$, the corresponding ZVSA accurately equals to zero. On the other hand, N_H is the intersection point between D_{min} and x-axis. Therefore, the horizontal coordinate of N_H is the upper limit frequency ω_{oH}. Then, the OOFR with $K_{cc} = 0.05$, is from ω_{oL} to ω_{oH}. When $K_{cc} = 0.05$, the WPTS will operate at any point of the red solid line between N_L and N_H where the primary inverter will always realize ZVS operation. The only difference in these points is the value of ZVSA. According to (9), the per-unit value of φ_{ZA} can be obtained by

$$\varphi_{ZApu} = \varphi_{IIApu} - D_{min}. \tag{38}$$

When ω_n gradually increases between ω_{oL} and ω_{oH}, φ_{ZA} gradually increases. Especially, when φ_{ZA} is controlled to be 30°, the system should operate at point N_1, which is shown in Fig. 9(b).

According to Table I, in CC charging mode, the R_L ranges from 8 to 18 Ω. When the constant charging current is set as 4 A with $V_1 = 80$ V, then $K_{cc} = 0.05$. With the parameters listed in Table II, φ_{ZApu}, φ_{IIApu}, and D_{min} with different R_L and k are plotted in Fig. 10. When R_L increases from 8 (R_{BTA}) to 18 Ω (R_{BTB}), the OOFR ranging from A_x to B_x ($x = 1 - 3$) gradually approaches $\omega_n = 1$. Similarly, by comparing Fig. 10(a) with (b), the OOFR also approaches $\omega_n = 1$ when k decreases.

$$D = \frac{2}{\pi}\arcsin\left[\frac{K_{cc}}{8kL_2\omega_n^3}\sqrt{L_1L_2\left(64R_L^2\omega_n^2(-1+\omega_n^2)^2 + \pi^4\omega_0^2L_2^2(-1+2\omega_n^2+(-1+k^2)\,\omega_n^4)^2\right)}\right] \tag{35}$$

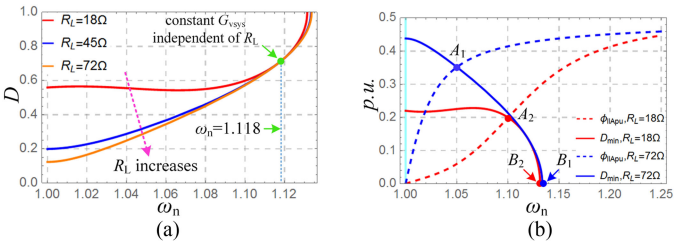

Fig. 11. (a) Relationship between D and $\omega_{\rm n}$, with $K_{\rm cv} = 0.9$ and $k = 0.2$. (b) Critical condition for ZVS and CV charging with $G_{\rm vsys} = 0.9$ and $k = 0.2$ when $R_{\rm L} = 18\ \Omega$ and $72\ \Omega$, respectively.

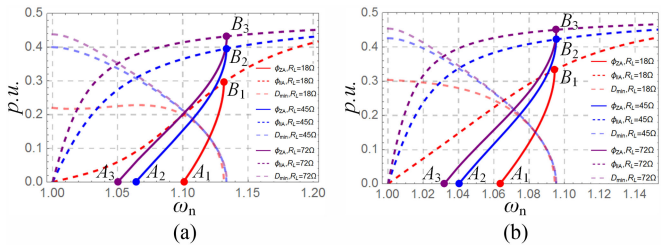

Fig. 12. OOFR is between $A_{\rm x}$ and $B_{\rm x}$ (x = 1, 2, 3), with $K_{\rm cv} = 0.9$, $R_{\rm L} = 18\ \Omega$, $45\ \Omega$, $72\ \Omega$. (a) $k = 0.2$. (b) $k = 0.15$.

B. CV Charging and ZVS Operation

Similarly, when the battery packs enter into the CV mode, the charging voltage of WPTS will maintain constant and $R_{\rm L}$ continues to increase as the charging process continues. When the input dc voltage V_1 and output voltage V_2 are constant, $K_{\rm cv}$ is constant. According to (16), if assigning that $G_{\rm vsys}$ equals $K_{\rm cv}$, then the corresponding duty cycle D can be solved by (39) as shown at bottom of the page.

With the parameters listed in Table I, to maintain $G_{\rm vsys}$ constant, the relationship curves between $\omega_{\rm n}$ and D are plotted in Fig. 11(a). When $R_{\rm L}$ increases, the control variable D decreases accordingly and the OFR $\omega_{\rm n}$ increases. In Fig. 11(b), in accordance with the CC mode, the optimal OFRs are from $A_{\rm x}$ to $B_{\rm x}$ ($x = 1, 2$), with $K_{\rm cv} = 0.9$ and $k = 0.2$ when $R_{\rm L} = 18\ \Omega$ and $72\ \Omega$. As $R_{\rm L}$ gradually increases, the upper limit frequency increases slowly and the lower limit frequency decreases relatively quickly because the designed CV point of resonant parameters is near the upper limit frequency. In a word, as $R_{\rm L}$ gradually increases, OOFR also gradually increases in CV mode. With the parameters listed in Table II, $\varphi_{\rm IIApu}$, $\varphi_{\rm ZApu}$, and $D_{\rm min}$ are plotted in Fig. 12. When $R_{\rm L}$ increases from 18($R_{\rm BTB}$) to 72 Ω($R_{\rm BTC}$), the OOFR ranging from $A_{\rm x}$ to $B_{\rm x}$ ($x = 1 \sim 3$) gradually approaches $\omega_{\rm n} = 1$. Similarly, by comparing Fig. 12(a) with (b), when k decreases, the OOFR also approaches $\omega_{\rm n} = 1$.

C. OOFR and the Maximum ZVSA

According to Fig. 10 and 12, the upper limits and lower limits of OOFR versus $R_{\rm L}$ can be calculated and plotted in Fig. 13(a).

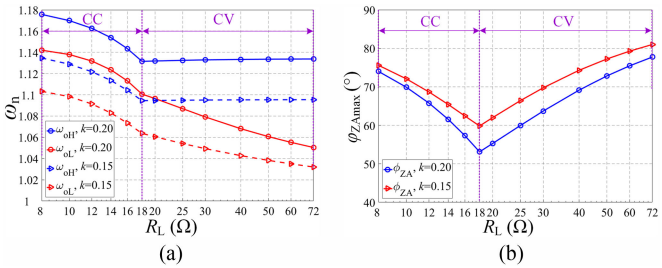

Fig. 13. OOFR and ZVSA versus load resistor $R_{\rm L}$ with $k = 0.15$ and 0.2, when $K_{\rm cc} = 0.05$ in CC mode and $K_{\rm cv} = 0.9$ in CV mode. (a) Upper and lower limits of OOFR versus $R_{\rm L}$ with different k. (b) Theoretical maximum ZVSA versus $R_{\rm L}$ with different k.

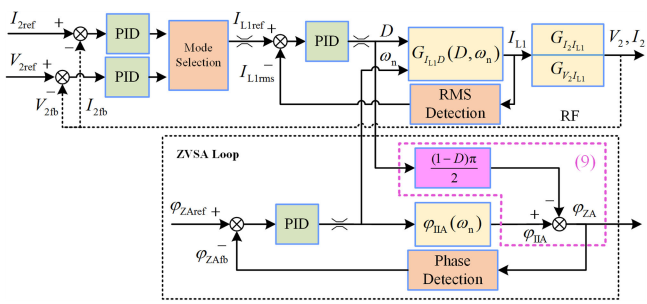

Fig. 14. System control structure.

When $G_{\rm ivsys}$ is controlled to be constant, the upper and lower limits of operation frequency $\omega_{\rm n}$ are closer to 1 with larger load $R_{\rm L}$ and lower coupling coefficient k. In Fig. 13(b), the theoretical maximum ZVSA can be calculated and plotted. In CC mode, when $R_{\rm L}$ increases, the theoretical maximum ZVSA will decrease and the opposite is true in CV mode.

V. Implementation of the Proposed TLCS

To verify OOFR and the proposed parameter design method, the vital step is to make the system operate at any point of OOFR freely. Therefore, a TLCS is proposed to realize CC/CV charging and accurate ZVSA control simultaneously. This paper mainly presents an implementation method of the proposed TLCS.

A. Description of TLCS

The control block diagram of TLCS is shown in Fig. 14. The control strategy is comprised of three closed loops: the inner loop of the rms value of primary resonant current, the outer loop of the CC output or CV output and the ZVSA loop of primary inverter. The basic idea of the TLCS has two basic aspects. One point is to control the output current or voltage by changing the phase shift angle $D\pi$. The other point is to change the IIA of the resonant network by adjusting the operation frequency of inverter to control the ZVSA. The operation principal and implementation of these loops are briefly explained as follows.

$$D = \frac{2}{\pi}\arcsin\left[\frac{K_{\rm cv}}{8kL_2R_{\rm L}\omega_{\rm n}^3}\sqrt{L_1L_2\left(64R_{\rm L}^2\omega_{\rm n}^2(-1+\omega_{\rm n}^2)^2+\pi^4\omega_0^2L_2^2(-1+2\omega_{\rm n}^2+(-1+k^2)\,\omega_{\rm n}^4)^2\right)}\right] \tag{39}$$

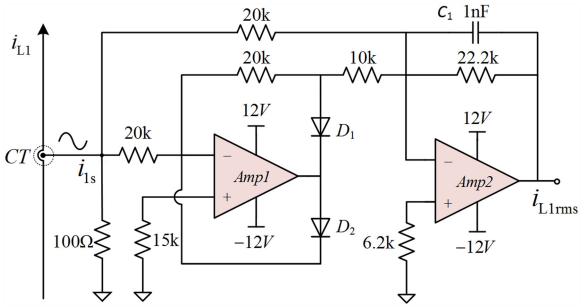

Fig. 15. Accurate rms detection circuit with two operational amplifiers.

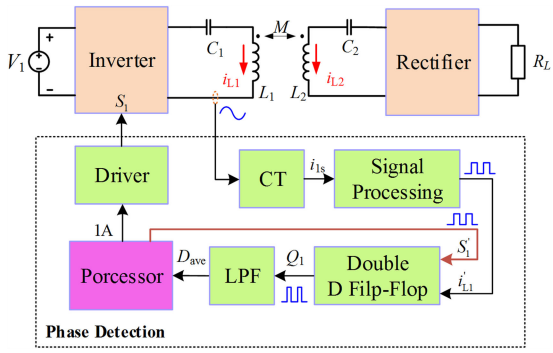

Fig. 16. Operation principle diagram of the phase detection method.

B. Operation Principal of TLCS

1) Inner Loop of Primary Resonant Current: As shown in Fig. 14, I_{L1ref} is the rms value instruction of the inner current loop of primary resonant current I_{L1}. The corresponding feedback signal I_{L1rms}, is detected by an analog circuit. In consideration of the accuracy and rapidity of the rms detection circuits, an operational amplifier (OPA)-based precision full-wave rectifier is carefully designed and adopted, which is shown in Fig. 15.

The aim of the inner current loop is to improve the dynamic response of the WPTS and to restrict the amplitude of primary resonant current to a safe operating region. As we all know, when ω_{n} approaches 1, the resonant network behaves as a CC source. However, in exceptional cases that the secondary load suddenly disconnects, it will lead to extreme dc output voltage that will destroy the system. Therefore, it is necessary to limit I_{L1rms} to a safe operating region. The processor of primary inverter samples I_{L1rms} and calculates phase shift angle of the primary inverter through the proportion integration differentiation (PID) algorithm.

2) Outer Loop of CC Charging or CV Charging: The output current reference $I_{2\mathrm{ref}}$ in the CC mode and output voltage reference $V_{2\mathrm{ref}}$ in the CV mode are preset instructions. The processor of secondary rectifier samples I_2 and V_2, and then sends them to the primary processor through radio frequency (RF2.4G) communication. Based on $V_{2\mathrm{ref}}$, $I_{2\mathrm{ref}}$ and $V_{2\mathrm{fb}}$, $I_{2\mathrm{fb}}$, the primary processor calculates the instructions of inner current loop through the PID algorithm respectively. After that, by comparing these two calculation results, the smaller one is used as the reference of inner current loop. Therefore, the control outer loop can realize the smooth switching from the CC mode to CV mode automatically.

3) Decoupled ZVSA Loop of Primary Inverter: To realize ZVS operation of primary inverter absolutely, φ_{ZA} must be controlled independently and it should be larger than zero. However, D changes for controlling CC or CV output in real time, which leads to the change of φ_{ZA} accordingly. Therefore, the phase loop and current loop are highly coupled. Fortunately, according to (9), a simple decoupled control for ZVSA loop is proposed, which is marked in bright purple line. Simultaneously, to decrease the effect of ZVSA loop to inner current loop, the setting time of ZVSA loop is relatively longer than that of inner current loop.

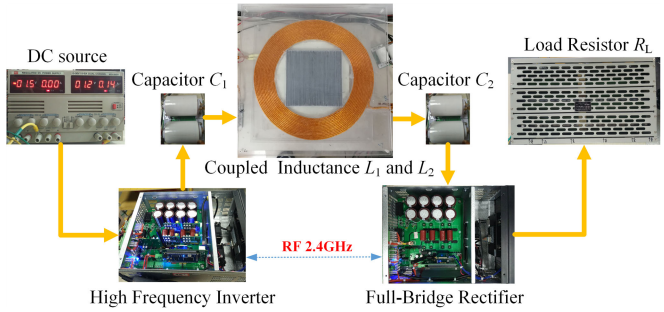

Fig. 17. Experimental prototype.

In the ZVSA loop, φ_{ZAref} is a variable reference angle for realizing ZVS and the corresponding feedback signal is φ_{ZAfb}, which is detected by phase detection method. The principle diagram of the phase detection method is shown in Fig. 16. $i_{1\mathrm{s}}$ is the current transformer output signal of primary resonant current i_{L1}. Next, a signal processing circuit is adopted to convert $i_{1\mathrm{s}}$ to square waveform i'_{L1}, which is in phase with i_{L1}. Then, the processor produces a reference signal S'_1, which is 180° leading to driver signal S_1. By using double D flip-flops, the signal Q_1 can be obtained and the duty cycle of Q_1 represents the phase of i_{L1}. Finally, by using a low-pass filter, the dc value of Q_1 can be acquired and sampled by DSP28335. The detailed analysis has been published in [28] and we will not repeat it.

Based on φ_{ZAref} and φ_{ZAfb}, the primary processor calculates the operation frequency of inverter through PID algorithm. By adjusting the operation frequency of the inverter, the IIA of the resonant network will be changed. According to Figs. 10 and 12, ZVSA is a monotonic increasing function of the operation frequency. Therefore, the ZVSA can be directly controlled by adjusting the operation frequency.

VI. Experimental Evaluation

A. Experimental Prototype

1) Main Power Circuit Design: To verify the previous analysis, a 500-W experimental prototype is built up, which is shown in Fig. 17. The prototype includes a dc source, a high frequency inverter, an SS resonant network, a full-bridge rectifier, and a sliding rheostat. Energy is transferred from dc source to sliding rheostat. The primary inverter is controlled by DSP28335. The

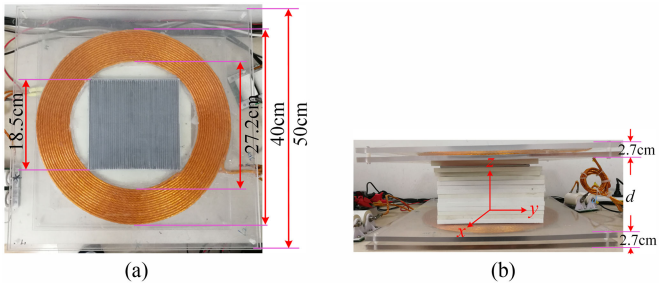

Fig. 18. Designed coils with 40 cm outer-loop diameter and 2.7 cm thickness. (a) Front view. (b) Side view.

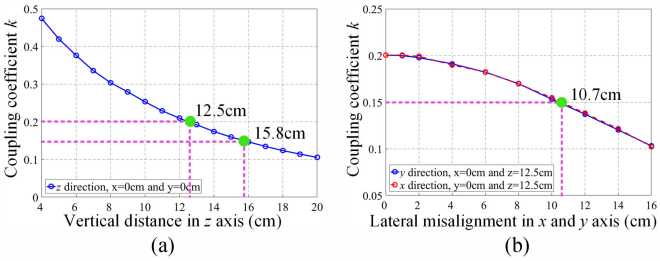

Fig. 19. Coupling coefficient of the two coils (measurement result). (a) Vertical distance in z-axis with $x = 0$ and $y = 0$. (b) Lateral misalignment in x- and y-axes with $z = 12.5$ cm.

TABLE V
PARAMETERS OF THE WPTS

Symbol	Quantity	Value
L_1	primary resonant inductor	118.43 μH
C_1	primary resonant capacitor	29.92 nF
f_1	primary resonant frequency	84.55 kHz
R_1	primary ESR	0.12 Ω
L_2	secondary resonant inductor	118.55 μH
C_2	secondary resonant capacitor	29.88 nF
f_2	secondary resonant frequency	84.56 kHz
R_2	secondary ESR	0.11 Ω
N_1, N_2	number of turns	15
R_{L}	load resistor	8 Ω – 72 Ω
d	distance of coils	12.5 cm – 15.8 cm
k	coupling coefficient	0.20 – 0.15

MOSFETs used in the inverter are IXTQ96N20P, and the antiparallel diodes of IXTQ96N20P are used for the secondary rectifier. The primary and secondary sides exchange signals and instructions by 2.4-GHz wireless communication modules. Both the coupled coils are made by Litz wire. The structure of windings is carefully designed to lower ESRs and to increase coupling coefficient. As shown in Fig. 18(a), the outer diameters of coils are 40 cm and the thicknesses are about 2.7 cm. The coupling coefficient of the two coils in different vertical and horizontal distances is measured by KEYSIGHT E4990A. The relationships between coupling coefficient and distance (in x, y, and z directions) are plotted in Fig. 19. The other detailed experimental parameters are listed in Table V.

2) Sampling Circuit Design: In the whole system, to realize TLCS, the sampling circuits are necessary, which mainly include two parts: the rms detection circuits and phase detection circuits. The whole sampling circuits are carefully designed and condensed into a PCB board, which is beneficial for achieving anti-interference performance. The hardware design board of the sampling circuits is shown in Fig. 20 with the each part emphasized by the yellow dashed rectangle.

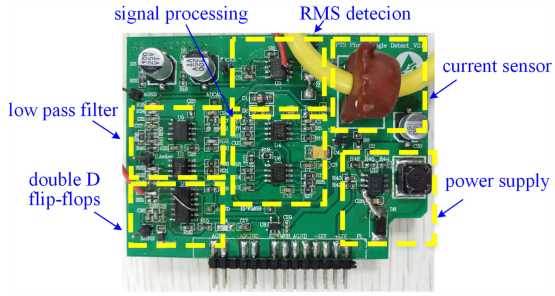

Fig. 20. Hardware design board of the sampling circuits.

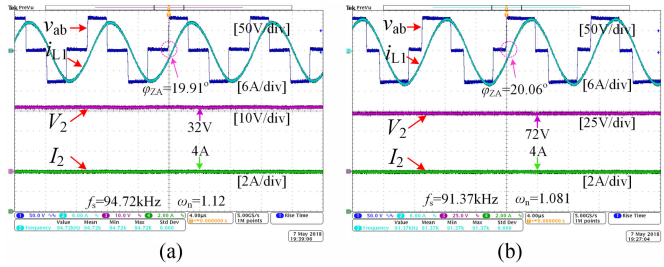

Fig. 21. Steady-state waveforms in CC mode for battery charging, when $V_1 = 80$ V, $I_2 = 4$ A, $K_{\mathrm{cc}} = 0.05$, $k = 0.15$, $\varphi_{\mathrm{ZAref}} = 20°$, (a)$R_{\mathrm{L}} = 8\,\Omega$, (b)$R_{\mathrm{L}} = 18\,\Omega$.

B. Steady-State Operation Waveforms

To verify the rationality of the designed parameters and the effectiveness of the proposed TLCS, the steady-state operation of the WPTS is investigated first. When the battery packs are in CC mode, the load resistor R_{L} is adjusted to equal R_{BTA} or R_{BTB}, which are used to simulate the practical charging process at the starting and terminal points of the CC charging mode of the preset battery packs. In CC mode, the TCGS is set as 0.05 (with the output current $I_2 = 4$ A) and the instruction of ZVSA, φ_{ZAref}, is set as 20°. The steady-state operation waveforms of the WPTS are shown in Fig. 21.

Similarly, when the battery packs are in CV mode, the load resistor R_{L} is adjusted to equal R_{BTB} or R_{BTC}, which are used to simulate the practical charging process at the starting and terminal points of CV mode of the preset battery packs. In the CV mode, VGS is set as 0.9 (with the output voltage $V_2 =$ 72 V) and the instruction of ZVSA, φ_{ZAref}, is set as 20°. The steady-state operation waveforms of the WPTS are shown in Fig. 22.

C. Verification of OOFR

To verify the analysis and calculated results of OOFR, the theoretical calculations and experimental measurements of OOFR are synthetically compared in different coupling coefficient k

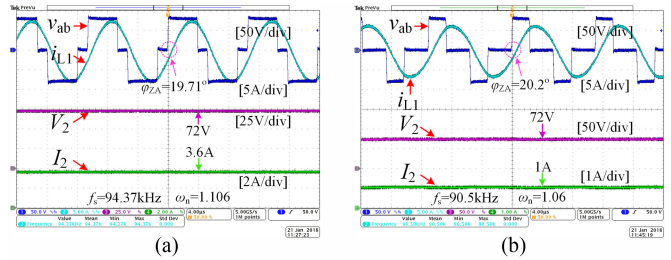

Fig. 22. Steady-state waveforms in CV mode for battery charging, when V_1 = 80 V, V_2 = 72 V, K_{cv} = 0.9, k = 0.2, φ_{ZAref} = 20°, (a) R_L = 20 Ω, (b) R_L = 72 Ω.

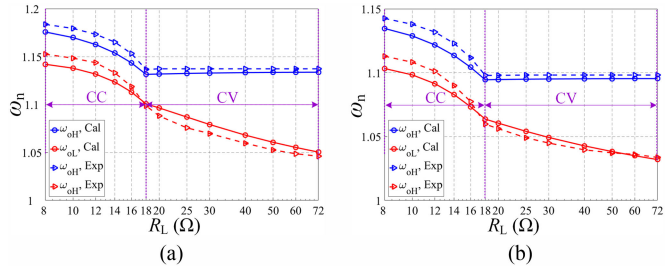

Fig. 23. Comparison of OOFR between theoretical calculations and experimental measurements in the whole battery charging process, when V_1 = 80 V, K_{cc} = 0.05 (CC mode) or K_{cv} = 0.9 (CV mode). (a) k = 0.2. (b) k = 0.15.

and load resistor R_L. By setting $\varphi_{ZAref} = 0°$ or $\varphi_{ZAref} = \varphi_{ZAmax}$ with different coupling coefficient, the upper side and lower side frequency points are calculated and measured in the whole charging process of the battery packs, which are shown in Fig. 23.

At the same time, the practical measured frequency points are plotted in an identical picture with dashed lines. We find that the experimental results are in good agreement with the calculated ones. In CC mode, OOFR moves toward $\omega_n = 1$ and their frequency widths are maintained constant approximately as R_L increases gradually. In CV mode, the upper side frequency points of OOFR maintain constant approximately and are independent of R_L, which is conform to the previous design. Meanwhile, the lower side frequency points of OOFR move toward $\omega_n = 1$, which makes OOFR wider as R_L increases.

The comparison of the maximum ZVSA between theoretical calculations and experimental measurements in the whole battery charging process with different coupling coefficient are shown in Fig. 24. In CC mode, the maximum ZVSA gradually decreases as R_L increases, and in CV mode, the maximum ZVSA gradually increases as R_L increases, which is also in accordance with the previous analysis. The experimental maximum values of ZVSA are smaller than the calculated ones because the theoretical calculation ignores the deadtime effect of inverter.

D. Verification of Parameter Design

To verify the rationality of parameter design, the resonant currents of coils and resonant voltages of capacitors are calculated and measured carefully. According to the previous analysis, we only consider the worst operation condition with the lowest coupling. In the whole charging process, the resonant currents of coils in the primary and secondary sides are calculated and measured with the upper and lower frequencies, respectively, which are shown in Fig. 25. The primary resonant current gradually increases and then decreases along the charging process. When $R_L = R_{BTB}$ (the starting point of CV mode) and $\omega_n = \omega_{oH}$, the primary resonant current I_{L1} achieves the maximum value in both the theoretical calculation and experimental measurement, which verifies the previous assumptions. The maximum values of I_{L1} in both calculation and experiment are all below the preset value I_{L1max}. The secondary resonant current I_{L2} is independent of the operation frequency and only depends on the output current, which also conforms to the previous analysis. In Fig. 26, the resonant voltages of the WPTS in the whole charging battery are given. The resonant voltages have the similar conclusions as the resonant currents and the maximum values

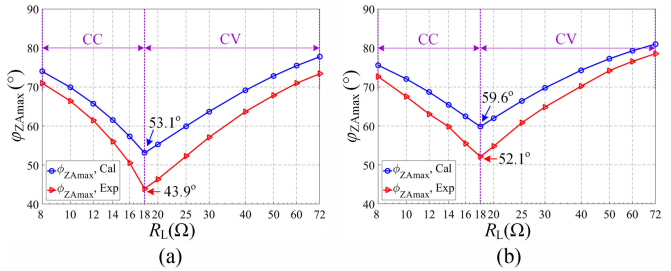

Fig. 24. Comparison of the maximum ZVSA between theoretical calculations and experimental measurements in the whole battery charging process, when V_1 = 80 V, K_{cc} = 0.05 (CC mode) or K_{cv} = 0.9 (CV mode). (a) k = 0.2. (b) k = 0.15.

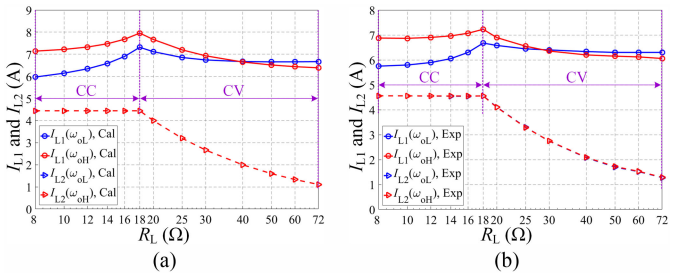

Fig. 25. Resonant current of WPTS, I_{L1} and I_{L2}, in the whole battery charging process when V_1 = 80 V, k = 0.15, K_{cc} = 0.05 (CC mode) or K_{cv} = 0.9 (CV mode). (a) Theoretical calculation results. (b) Experimental measurement results.

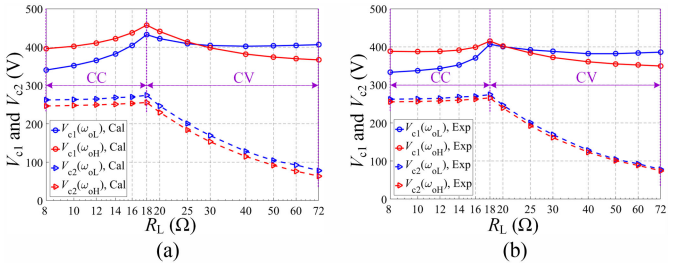

Fig. 26. Resonant voltage of the WPTS, V_{c1} and V_{c2}, in the whole battery charging process when V_1 = 80 V, k = 0.15, K_{cc} = 0.05 (CC mode) or K_{cv} = 0.9 (CV mode). (a) Theoretical calculation results. (b) Experimental measurement results.

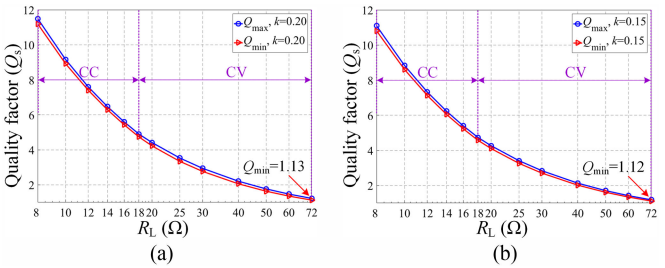

Fig. 27. Comparison of quality factor Q_s in the whole battery charging process with different R_L. (a) $k = 0.20$. (b) $k = 0.15$.

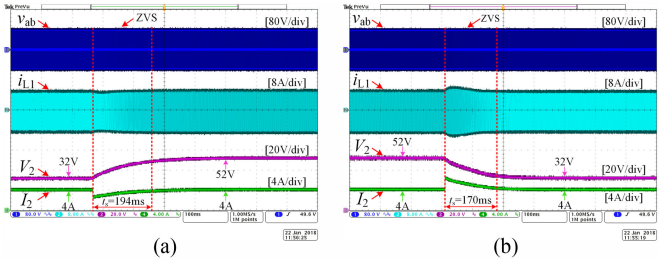

Fig. 28. Dynamic waveforms with changing R_L, when $V_1 = 80$ V, $I_2 = 4$ A, $k = 0.15$, $\varphi_{ZA} = 20°$. (a) Changing R_L from 8 to 13 Ω. (b) Changing R_L from 13 to 8 Ω.

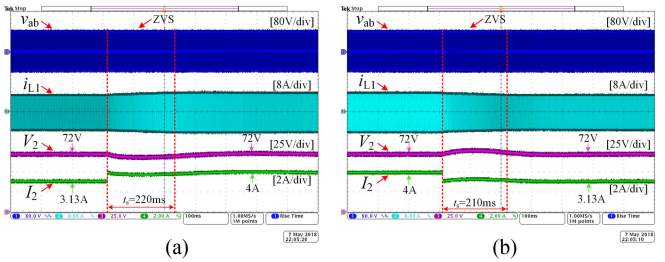

Fig. 29. Dynamic waveforms with changing R_L, when $V_1 = 80$ V, $V_2 = 72$ V, $k = 0.2$, $\varphi_{ZA} = 20°$. (a) Changing R_L from 23 to 18 Ω. (b) Changing R_L from 18 to 23 Ω.

of the calculation and experiment are below the preset values V_{c1max} and V_{c2max}.

As shown in Fig. 27, the quality factors of the designed WPTS versus R_L are measured in the whole charging process with different coupling coefficient. In OOFR, as R_L gradually increases, the maximum and minimum values of Q_s also gradually decrease. When $R_L = 72$ Ω (R_{BTC}) and $k = 0.15$, the minimum value of Q_s is 1.12 (larger than 1), which conforms to the previous design.

E. Dynamic Performance of TLCS

To verify the dynamic response of the proposed TLCS, the step changes of the load resistor in CC and CV modes are tested. In CC mode, Fig. 28 shows the dynamic responses by changing R_L between 8 and 13 Ω suddenly, under condition of maintaining $I_2 = 4$ A and $\varphi_{ZA} = 20°$, with $V_1 = 80$ V and $k = 0.15$. The dynamic setting times are 194 and 170 ms, respectively. In CV mode, Fig. 29 shows the dynamic responses

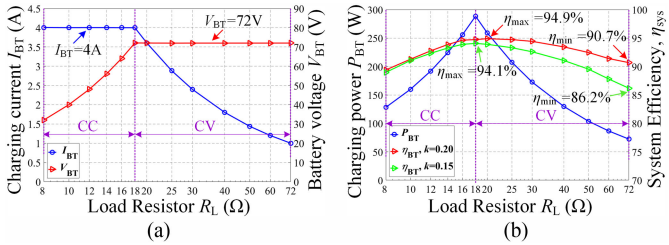

Fig. 30. Charging experiments simulated by a sliding rheostat with $\varphi_{ZAref} = 7°$. (a) Charging current and voltage versus R_L with $k = 0.2$. (b) Charging power and system efficiency versus R_L with $k = 0.2$ or $k = 0.15$.

by changing R_L between 18 and 23 Ω suddenly, under condition of maintaining $V_2 = 72$ V and $\varphi_{ZA} = 20°$, with $V_1 = 80$ V and $k = 0.2$. The dynamic setting times are 220 and 210 ms, respectively. The primary inverter can realize ZVS operation completely in the dynamic process, which is beneficial to the safe and stable operation of WPTS.

F. Charging Efficiency of WPTS

By changing the resistance of sliding rheostat to simulate the whole charging process, the designed WPTS will power the varying load in CC mode or CV mode with $\varphi_{ZAref} = 7°$. The charging current and voltage curves of the battery packs are shown in Fig. 30(a). In Fig. 30(b), the charging power gradually increases in the CC mode and gradually decreases in the CV mode. The system maximum efficiency can achieve 94.9% and 94.1% with $k = 0.2$ and $k = 0.15$ near the maximum output power.

G. Comparison With Other Reported WPTS

The system transfer efficiencies in some published papers are summarized. Table VI compares the WPT prototype in this paper with the representative reported WPTSs. The key parameters, including coil diameter, power transfer distance, coupling coefficient, transfer power, and system efficiency, are listed in this table. To compare the transfer efficiency more reasonably and based on this paper, the resonant frequency should be limited to 1 MHz and the transfer power should be limited to 1 kW. Take the coil size and the transfer distance into account, a normalized distance D_{nom} is defined as transfer distance over coil diameter [39], [40], which is

$$D_{nom} = d/\sqrt{D_1 \times D_2} \tag{40}$$

where D_1 and D_2 are the diameters of the primary and secondary coils, respectively. The normalized distance is considered because it is the major limiting factor on the efficiency.

Fig. 31 shows the system transfer efficiency with respect to the normalized distance. It can be seen from Fig. 31 that when the normalized distance is larger, the lower efficiency can be achieved in any of WPTS. The prototype in this paper can achieve higher efficiency at the same normalized distance, and provide larger normalized distance for the same efficiency.

TABLE VI
PERFORMANCE COMPARISON OF THE WPTS

No	Paper reference	Tx Coil Size (mm)	Rx Coil Size (mm)	Distance d (mm)	Normalized Distance	Coupling Coefficient	Transfer Power P_o (W)	Efficiency (%)
1	[26]	380	380	150	0.39	0.26	400	82
				200	0.53	n/a	400	79
2	[35]	270	270	100	0.37	0.18	25	87
				150	0.56	0.10	25	83
3	[39]	300	300	100	0.33	0.23	10	93
				200	0.67	0.08	10	89
4	[40]	125	115	55	0.46	0.14	10	76
5	[41]	43	43	23.5	0.55	n/a	5	73
6	[42]	88	88	25	0.28	0.25	90	89.5
				33	0.38	0.17	90	86.5
7	[43]	310	310	200	0.65	0.07	7	73
8	[44]	420	420	100	0.24	0.13	∼1000	91.3
9	[45]	1000	1000	700	0.7	0.031	100	70
10	[46]	>200	>200	60	<0.3	0.277	200	88
11	[47]	200	200	130	0.65	n/a	10	80.2
12	*OurPaper*	400	400	125	0.31	0.20	288	94.9
				158	0.4	0.15	288	94.1

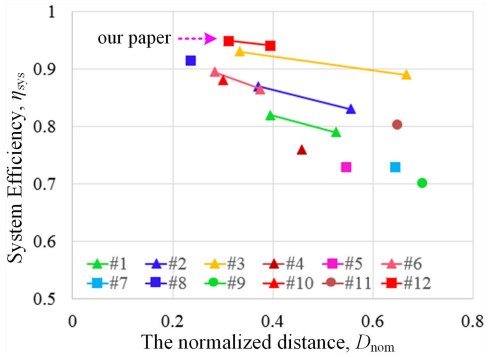

Fig. 31. Efficiency comparison of the WPTSs listed in Table VI.

VII. CONCLUSION

This paper investigates OOFR to realize the constant output and ZVS operation of inverter in the WPTS. With the purpose of obtaining OOFR, an optimized electrical parameter design method based on VFPSC is proposed with the multiple boundary conditions. Moreover, an implementation method of the novel TLCS is put forward to make the system operate at any point of OOFR accurately. Benefiting from the proposed TLCS, the whole system can realize ZVS in the whole charging process not only in the steady state, but also in the dynamic process. The WPTS can achieve the maximum efficiency 94.9% with $k = 0.2$ and 94.1% with $k = 0.15$ near the maximum output power.

REFERENCES

[1] D. Ahn and S. Hong, "Wireless power transmission with self-regulated output voltage for biomedical implant," *IEEE Trans. Ind. Electron.*, vol. 61, no. 5, pp. 2225–2235, May 2014.

[2] H. M. Lee, H. Park, and M. Ghovanloo, "A power-efficient wireless system with adaptive supply control for deep brain stimulation," *IEEE J. Solid-State Circuits*, vol. 48, no. 9, pp. 2203–2216, Sep. 2013.

[3] H. Liu, Q. Shao, and X. Fang, "Modeling and optimization of class-e amplifier at subnominal condition in a wireless power transfer system for biomedical implants," *IEEE Trans Biomed. Circuits Syst*, vol. 11, no. 1, pp. 35–43, Feb. 2017.

[4] S. Stoecklin, A. Yousaf, T. Volk, and L. Reindl, "Efficient wireless powering of biomedical sensor systems for multichannel brain implants," *IEEE Trans. Instrum. Meas.*, vol. 65, no. 4, pp. 754–764, Apr. 2016.

[5] S. H. Lee, J. H. Lee, and K. P. Yi, "A new design methodology for a 1 meter distance, 6.78 MHz wireless power supply system for telemetries," in *Proc. Energy Convers. Congr. Expo.*, 2017, pp. 1–7.

[6] S. Y. R. Hui and W. W. C. Ho, "A new generation of universal contactless battery charging platform for portable consumer electronic equipment," *IEEE Trans. Power Electron.*, vol. 20, no. 3, pp. 620–627, May 2004.

[7] X. Liu and S. Y. Hui, "Simulation study and experimental verification of a universal contactless battery charging platform with localized charging features," *IEEE Trans. Power Electron.*, vol. 22, no. 6, pp. 2202–2210, Nov. 2007.

[8] Z. Cheng, Y. Lei, K. Song, and C. Zhu, "Design and loss analysis of loosely coupled transformer for an underwater high-power inductive power transfer system," *IEEE Trans. Magn.*, vol. 51, no. 7, pp. 1–10, Jul. 2015.

[9] A. Askari, R. Stark, J. Curran, D. Rule, and K. Lin, "Underwater wireless power transfer," in *Proc. Wireless Power Transfer Conf.*, 2015, pp. 1–4.

[10] Z. Wang, X. Wei, and H. Dai, "Nested three-layer optimisation method for magnetic coils used in 3 kw vehicle-mounted wireless power transfer system," *IET Power Electron.*, vol. 9, no. 13, pp. 2562–2570, 2016.

[11] R. Bosshard and J. W. Kolar, "Multi-objective optimization of 50 kw/85 khz IPT system for public transport," *IEEE J. Emerg. Sel. Topics Power Electron.*, vol. 4, no. 4, pp. 1370–1382, Dec. 2016.

[12] R. Bosshard, J. W. Kolar, J. Muhlethaler, and I. Stevanovic, "Modeling and eta - $alpha$ -pareto optimization of inductive power transfer coils for electric vehicles," *IEEE J. Emerg. Sel. Topics Power Electron.*, vol. 3, no. 1, pp. 50–64, Mar. 2015.

[13] Y. Jiang *et al.*, "An optimal parameters design methodology of series-series resonant tank of wireless power transmission system for battery charging," in *Proc. Appl. Power Electron. Conf. Expo.*, 2017, pp. 1600–1605.

[14] F. Lu, H. Zhang, H. Hofmann, W. Su, and C. Mi, "A dual-coupled LCC-compensated IPT system with a compact magnetic coupler," *IEEE Trans. Power Electron.*, vol. 33, no. 7, pp. 6391–6402, Jul. 2018.

[15] T. Kan, T. D. Nguyen, J. C. White, R. K. Malhan, and C. C. Mi, "A new integration method for an electric vehicle wireless charging system using LCC compensation topology: Analysis and design," *IEEE Trans. Power Electron.*, vol. 32, no. 2, pp. 1638–1650, Feb. 2017.

[16] S. Zhou and C. C. Mi, "Multi-paralleled LCC reactive power compensation networks and their tuning method for electric vehicle dynamic wireless charging," *IEEE Trans. Ind. Electron.*, vol. 63, no. 10, pp. 6546–6556, Oct. 2016.

[17] R. Bosshard and J. W. Kolar, "Inductive power transfer for electric vehicle charging: Technical challenges and tradeoffs," *IEEE Power Electron. Mag.*, vol. 3, no. 3, pp. 22–30, Sep. 2016.

[18] X. Qu, W. Zhang, S. C. Wong, and C. K. Tse, "Design of a current-source-output inductive power transfer led lighting system," *IEEE J. Emerg. Sel. Topics Power Electron.*, vol. 3, no. 1, pp. 306–314, Mar. 2015.

[19] C. Zhao, X. Xie, and S. Liu, "Multioutput led drivers with precise passive current balancing," *IEEE Trans. Power Electron.*, vol. 28, no. 3, pp. 1438–1448, Mar. 2013.
[20] X. Qu, S. C. Wong, K. T. Chi, and G. Zhang, "Design consideration of a current-source-output inductive power transfer led lighting system," in *Proc. Energy Convers. Congr. Expo.*, 2014, pp. 3607–3611.
[21] Y. C. Su, S. Y. Jeong, B. W. Gu, G. C. Lim, and C. T. Rim, "Ultraslim s-type power supply rails for roadway-powered electric vehicles," *IEEE Trans. Power Electron.*, vol. 30, no. 11, pp. 6456–6468, Nov. 2015.
[22] A. Zaheer, H. Hao, G. A. Covic, and D. Kacprzak, "Investigation of multiple decoupled coil primary pad topologies in lumped IPT systems for interoperable electric vehicle charging," *IEEE Trans. Power Electron.*, vol. 30, no. 4, pp. 1937–1955, Apr. 2015.
[23] C. Park, S. Lee, S. Y. Jeong, G. H. Cho, and C. T. Rim, "Uniform power i-type inductive power transfer system with dq-power supply rails for on-line electric vehicles," *IEEE Trans. Power Electron.*, vol. 30, no. 11, pp. 6446–6455, Nov. 2015.
[24] C. C. Mi, G. Buja, Y. C. Su, and C. T. Rim, "Modern advances in wireless power transfer systems for roadway powered electric vehicles," *IEEE Trans. Ind. Electron.*, vol. 63, no. 10, pp. 6533–6545, Oct. 2016.
[25] X. Qu, H. Han, S. C. Wong, K. T. Chi, and W. Chen, "Hybrid IPT topologies with constant current or constant voltage output for battery charging applications," *IEEE Trans. Power Electron.*, vol. 30, no. 11, pp. 6329–6337, Nov. 2015.
[26] G. Buja, M. Bertoluzzo, and K. N. Mude, "Design and experimentation of WPT charger for electric city car," *IEEE Trans. Ind. Electron.*, vol. 62, no. 12, pp. 7436–7447, Dec. 2015.
[27] K. Yan, Q. Chen, H. Jia, X. Ren, L. Cao, and R. Xinbo, "Self-oscillating contactless resonant converter with phase detection contactless current transformer," *Proc. CSEE*, vol. 29, no. 8, pp. 4438–4449, 2014.
[28] Y. Jiang, L. Wang, Y. Wang, J. Liu, X. Li, and G. Ning, "Analysis, design and implementation of accurate ZVS angle control for EV's battery charging in wireless high power transfer," *IEEE Trans. Ind. Electron.*, to be published, doi: 10.1109/TIE.2018.2795523.
[29] Y. Jiang, Y. Wang, J. Liu, X. Li, and L. Wang, "An accurate phase detection method for realizing ZVS of high frequency inverter in wireless power transmission," in *Proc. Future Energy Electron. Conf. ECCE Asia*, 2017, pp. 1380–1384.
[30] X. Qu, S. C. Wong, and K. T. Chi, "Contactless electronic ballast for high brightness led lamps with positionally dimmed method," in *Proc. Energy Convers. Congr. Expo.*, 2012, pp. 443–447.
[31] Q. Chen, S. C. Wong, C. K. Tse, and X. Ruan, "Analysis, design, and control of a transcutaneous power regulator for artificial hearts," *IEEE Trans. Biomed. Circuits Syst.*, vol. 3, no. 1, pp. 23–31, Feb. 2009.
[32] K. Song, Z. Li, Z. Du, G. Wei, and C. Zhu, "Design for constant output voltage and current controllability of primary side controlled wireless power transfer system," in *Proc. Emerg. Technologies: Wireless Power Transfer*, 2017, pp. 1–6.
[33] L. Xu, Q. Chen, X. Ren, S. C. Wong, and K. T. Chi, "Self-oscillating resonant converter with contactless power transfer and integrated current sensing transformer," *IEEE Trans. Power Electron.*, vol. 32, no. 6, pp. 4839–4851, Jun. 2017.
[34] T. D. Yeo, D. S. Kwon, S. T. Khang, and J. W. Yu, "Design of maximum efficiency tracking control scheme for closed-loop wireless power charging system employing series resonant tank," *IEEE Trans. Power Electron.*, vol. 32, no. 1, pp. 471–478, Jan. 2017.
[35] H. Li, J. Li, K. Wang, and W. Chen, "A maximum efficiency point tracking control scheme for wireless power transfer systems using magnetic resonant coupling," *IEEE Trans. Power Electron.*, vol. 30, no. 7, pp. 3998–4008, Jul. 2015.
[36] D. Ahn and S. Hong, "Wireless power transfer resonance coupling amplification by load-modulation switching controller," *IEEE Trans. Ind. Electron.*, vol. 62, no. 2, pp. 898–909, Feb. 2015.
[37] W. Zhang, S. C. Wong, K. T. Chi, and Q. Chen, "Design for efficiency optimization and voltage controllability of series–series compensated inductive power transfer systems," *IEEE Trans. Power Electron.*, vol. 29, no. 1, pp. 191–200, Jan. 2014.
[38] Y. Jiang, J. Liu, X. Hu, L. Wang, Y. Wang, and G. Ning, "An optimized frequency and phase shift control strategy for constant current charging and zero voltage switching operation in series-series compensated wireless power transmission," in *Proc. IEEE Energy Convers. Congr. Expo.*, 2017, pp. 961–966.
[39] H. Li, K. Wang, J. Fang, and Y. Tang, "Pulse density modulated ZVS full-bridge converters for wireless power transfer systems," *IEEE Trans. Power Electron.*, to be published, doi: 10.1109/TPEL.2018.2812213.
[40] D. Ahn, S. Kim, J. Moon, and I. K. Cho, "Wireless power transfer with automatic feedback control of load resistance transformation," *IEEE Trans. Power Electron.*, vol. 31, no. 11, pp. 7876–7886, Nov. 2016.
[41] X. Tang, J. Zeng, P. P. Kong, S. Mai, C. Zhang, and Z. Wang, "Low-cost maximum efficiency tracking method for wireless power transfer systems," *IEEE Trans. Power Electron.*, vol. 33, no. 6, pp. 5317–5329, Jun. 2018.
[42] Z. Huang, S. C. Wong, and K. T. Chi, "Control design for optimizing efficiency in inductive power transfer systems," *IEEE Trans. Power Electron.*, vol. 33, no. 5, pp. 4523–4534, May 2018.
[43] W. Zhong and S. Y. R. Hui, "Maximum energy efficiency operation of series-series resonant wireless power transfer systems using on-off keying modulation," *IEEE Trans. Power Electron.*, vol. 33, no. 4, pp. 3595–3603, Apr. 2018.
[44] A. Kamineni, G. A. Covic, and J. T. Boys, "Analysis of coplanar intermediate coil structures in inductive power transfer systems," *IEEE Trans. Power Electron.*, vol. 30, no. 11, pp. 6141–6154, Nov. 2015.
[45] E. S. Lee, B. G. Choi, S. C. Jin, D. T. Nguyen, and C. T. Rim, "Wide-range adaptive IPT using dipole-coils with a reflector by variable switched capacitance," *IEEE Trans. Power Electron.*, vol. 32, no. 10, pp. 8054–8070, Oct. 2017.
[46] Y. H. Sohn, H. C. Bo, E. S. Lee, G. C. Lim, G. H. Cho, and C. T. Rim, "General unified analyses of two-capacitor inductive power transfer systems: Equivalence of current-source SS and SP compensations," *IEEE Trans. Power Electron.*, vol. 30, no. 11, pp. 6030–6045, Nov. 2015.
[47] H. C. Bo, E. S. Lee, H. Jin, and C. T. Rim, "Lumped impedance transformers for compact and robust coupled magnetic resonance systems," *IEEE Trans. Power Electron.*, vol. 30, no. 11, pp. 6046–6056, Nov. 2015.

Yongbin Jiang (S'15) was born in Jiangsu, China, in 1990. He received the B.S. degree in electrical automatization from Jiangsu University, Jiangsu, China, in 2012 and the M.S. degree in instrument science and technology from Xi'an Jiaotong University, Xi'an, China, in 2015. He is currently working toward the Ph.D. degree in electrical engineering in Xi'an Jiaotong University, Xi'an.

His research interests include wireless power transfer, high frequency and high power density dc–dc converters, signal processing, and digital control technology.

Laili Wang (S'07–M'13–SM'15) was born in Shaanxi province, China, in 1982. He received the B.S., M.S., and Ph.D. degrees in electrical engineering from Xi'an Jiaotong University, Xi'an, China, in 2004, 2007, and 2011, respectively.

Since 2011, he has been a Postdoctoral Research Fellow with the Electrical Engineering Department, Queen's University, Kingston, ON, Canada. From 2014 to 2017, he was an Electrical Engineer with Sumida, Canada. In 2017, he joined Xi'an Jiaotong University as a Professor. His research interests include package and integration of passive devices in high frequency high power density dc–dc converters, wireless power transfer, and energy harvesting.

Yue Wang (M'05) received the B.S. degree from Xi'an Jiaotong University, Xi'an, China, in 1994, the M.S. degree from Beijing Jiaotong University, Beijing, China, in 2000, and the Ph.D. degree from Xi'an Jiaotong University, in 2003, all in electrical engineering.

He is currently a Full Professor with the School of Electrical Engineering, Xi'an Jiaotong University. His research interests include wireless power transfer, active power filters, multilevel converters, and HVDC.

Junwen Liu was born in Jiangxi, China, in 1994. He received the B.S. degree in electrical engineering from Xi'an Jiaotong University, Xi'an, China, in 2015. He is currently working toward the M.S. degree in electrical engineering in Xi'an Jiaotong University, Xi'an.

His research interests include wireless power transfer and high frequency high power density dc–dc converters.

Min Wu was born in Sichuan, China, in 1995. He received the B.S. degree in electrical automatization from Chongqing University, Chongqing, China, in 2017. He is currently working toward the M.S. degree in instrument science and technology in Xi'an Jiaotong University, Xi'an, China.

His research interests include wireless power transfer, high frequency and high power density dc–dc converters, signal processing, and digital control technology.

Gaidi Ning was born in Shaanxi province, China, in 1964. She received the B.S., M.S., and Ph.D. degrees in electrical engineering from Xi'an Jiaotong University, Xi'an, China, in 1986, 1994, and 2009, respectively.

She is long engaged in courses of classroom teaching and experimental teaching of digital electronic technology, and the updating of the experimental platform, experimental contents, teaching contents, and related teaching material. Her research interests include wireless power transfer and digital electronic technique.